



# Study of the slope deformation characteristics and landslide mechanisms under alternating excavation and rainfall disturbance

Xiang Yu<sup>1</sup> · Bin Gong<sup>1,2</sup> · Chun'an Tang<sup>1</sup>

Received: 22 January 2021 / Accepted: 4 July 2021 / Published online: 17 July 2021  
© Springer-Verlag GmbH Germany, part of Springer Nature 2021

## Abstract

To investigate slope stability under alternating excavation and rainfall disturbance and to reveal the intrinsic mechanism of the slope stress diffusion process caused by stress-seepage coupling, a method consisting of separate simulation of the excavation stress field and rainfall seepage field and superposition analysis is proposed. Meanwhile, the distribution of the pore water pressure and transient saturation zone in the AK2+210~AK2+610 section slope of a highway in Guangdong Province, China, is comprehensively analysed by calculating the rainfall seepage field during the excavation process. The effects of the rainfall seepage and slope stresses are further studied by applying the changing natural/saturated physical and mechanical parameters and pore water pressure values obtained by physical testing and parameter inversion. Moreover, the safety and stability of the highway slope during each stage is computed numerically using the strength reduction method, and the slope failure process, instability-inducing factors and failure mechanism are discussed in detail. The results indicate that the proposed separate simulation and superposition analysis method is effective and of considerable practical value in slope engineering. Additionally, a comprehensive slope stability treatment is suggested, which can be used as a reference for other slope projects experiencing alternating excavation and rainfall disturbance.

**Keywords** Slope instability · Alternating excavation and rainfall · Seepage field · Stress-seepage coupling · Numerical simulation

## Introduction

In slope engineering, excavation and rainfall are recognised as two of the main factors that cause slope instability (Sun et al. 2019; Zhao et al. 2019; Li et al. 2019; Han et al. 2021). The stress field adjustment and rock-soil mass deformation triggered by excavation unloading may result in primary crack expansion and new crack generation in the slope. Meanwhile, rainfall infiltration can promote the propagation of cracks, increase the rock-soil mass weight, and reduce the rock-soil mass shear strength (Li et al. 2020; Fu et al. 2020). For example, on September 17, 2011, a landslide occurred in Bailu village, Xi'an city, Shaanxi Province, China; 32 people were killed, and the following excessive excavation caused

stress field redistribution and induced trans-scale cracks, which were then enlarged by the continuous infiltration of rainwater (Zhuang and Peng 2014). From 2011 to 2012, the Linfen-Jixian Expressway project in Shanxi Province, China, suffered multiple landslides and geological disasters due to intensive excavation and rainfall, which seriously affected safety and delayed the progress of construction (Wang et al. 2014). In 2014, a large-scale landslide occurred in Fuquan County, Guizhou Province, China; 23 people were killed, 22 people were injured, and 77 houses were damaged. The unfavourable geological structure of the slope was the determining factor, and excavation and continuous rainfall were the triggering factors that induced the landslide (Lin et al. 2018). The abovementioned cases show that slope instability caused by alternating excavation and rainfall has become a major engineering problem because it not only causes large economic losses but also seriously threatens civilian life safety.

As a challenging topic in the geotechnical engineering field, slope stability analysis under alternating excavation and rainfall conditions requires an in-depth consideration of stress and seepage. At present, slope stability studies

✉ Bin Gong  
gongbin@dlut.edu.cn

<sup>1</sup> State Key Laboratory of Coastal & Offshore Engineering, Dalian University of Technology, Dalian 116024, China

<sup>2</sup> Department of Civil and Environmental Engineering, Brunel University London, London UB8 3PH, UK

considering the stress and seepage effects can be divided into two categories. In the first category of studies, a coupling analysis of seepage and stress fields is conducted, and the direct interaction between them is studied. For example, Kim et al. (2016) established a two-dimensional hydraulic coupling infiltration model to study the infiltration of a series of soil columns with different properties and analyse the matric suction and effective stress of unsaturated soil slopes. Liu et al. (2017) established a fluid–solid coupling constitutive equation based on the single variable effective stress theory of unsaturated soils and further analysed a red clay embankment slope of the Dazhou-Chengdu Railway in Sichuan Province, China, by considering rainfall, groundwater seepage, and fluid–solid coupling. They pointed out that the key factors affecting slope stability are the intensity and duration of rainfall and soil long-term strength indices. Robinson et al. (2017) used a nonstationary climate simulation method to obtain the baseline (historical) and predicted (future) precipitation extremes in the study area and integrated them into a series of fully coupled two-dimensional (2D) stress unsaturated flow simulations to compare the response of the baseline model and the predicted model during 7 days of continuous rainfall. However, since fluid–solid coupling analysis is very complicated, the effect of engineering excavation is generally not considered in the first category of studies. In the other category of studies, seepage and stress are treated separately, and the seepage calculation results (e.g. pore water pressure and effective parameters) are directly applied to the stress elements to analyse slope stresses under rainwater infiltration. For example, Lu et al. (2012) described a method to quantify the safety factor's scalar field based on the concept of Coulomb stress and studied the shift of the stress state towards the critical failure state that results from rainfall infiltration. Oh and Lu (2015) used a generalised effective stress framework to extend the methods of limit equilibrium and finite element analysis to unsaturated conditions and then applied the recorded rainfall, measured shear strength parameters, soil–water retention curve, and site geology to reproduce the failure events of two engineering slopes due to rainfall.

In fact, the seepage–stress separation method can simulate the slope excavation–rainfall coupling process by analysing the excavation stress field first and then imposing rainfall on the formed boundary. For instance, Li et al. (2017) used discrete element simulation to study the deformation characteristics and failure mechanism of a steep rock slope in the Wulong area of Chongqing city, China, under excavation and rainfall; Taga et al. (2015) back-analysed the failure process of an engineering slope affected by rainfall along the Mersin-Tarsus Expressway in Turkey, estimated the soil effective shear strength and determined the slope failure mechanism. However, the current separation method is incompetent for slope stability analysis under alternating excavation and

rainfall conditions (i.e. the excavation–rainfall–excavation process). The main difficulties lie in unsaturated soil slope excavation simulation during the rainfall–excavation process. Due to the pore water in unsaturated soil slopes, the seepage field and stress field cannot be separated in a direct manner. Excavation will change the seepage paths and cause water to seep out, which causes the entire seepage field to change, and the dissipation of pore water pressure will change the stress field by increasing the soil effective stress. However, pore pressure dissipation is a delayed process, and excavation is an instantaneous unloading process. Therefore, it is difficult to directly couple the two processes on the time domain, which makes numerical simulation difficult.

In this study, a simulation and superposition analysis method that treats the excavation stress field and rainfall seepage field separately is developed by taking the dissipation of pore water pressure during unsaturated slope excavation and the shear strength parameter weakening in the saturated zone into consideration. Slope stability analysis under alternating excavation and rainfall conditions is realised by solving the difficulty of numerically simulating unsaturated slope excavation. The slope failure process of a highway slope in Guangdong Province, China, is simulated using the saturated shear strength parameters of rock and soil materials obtained by parameter inversion. The effectiveness and accuracy of the proposed method is therefore verified. Additionally, the role of slope instability-inducing factors is analysed, and the slope failure mechanism under alternating excavation and rainfall conditions is comprehensively discussed.

## Alternating excavation and rainfall analysis method

### Unsaturated slope excavation simulation difficulty

This section will explain the simulation difficulty of unsaturated slope excavation. Figure 1 shows the change in the seepage field of an unsaturated soil slope because of rainfall infiltration before and after excavation. Before excavation, the seepage surface is assumed to coincide with the bottom boundary, and rainfall intensity  $q$  is applied to the top boundary. The rainwater infiltrates from the top and seeps towards the bottom. After excavation, the infiltration boundary of the excavation area disappears, and the excavation–formed boundary becomes a new seepage surface. The rainwater near the excavation boundary seeps towards the new surface, while the rest still seeps towards the bottom. Thus, the seepage paths are changed by excavation.

In other words, excavation changes the seepage paths in the slope, which changes the pore water pressure and distribution in saturated–unsaturated regions. This process lags

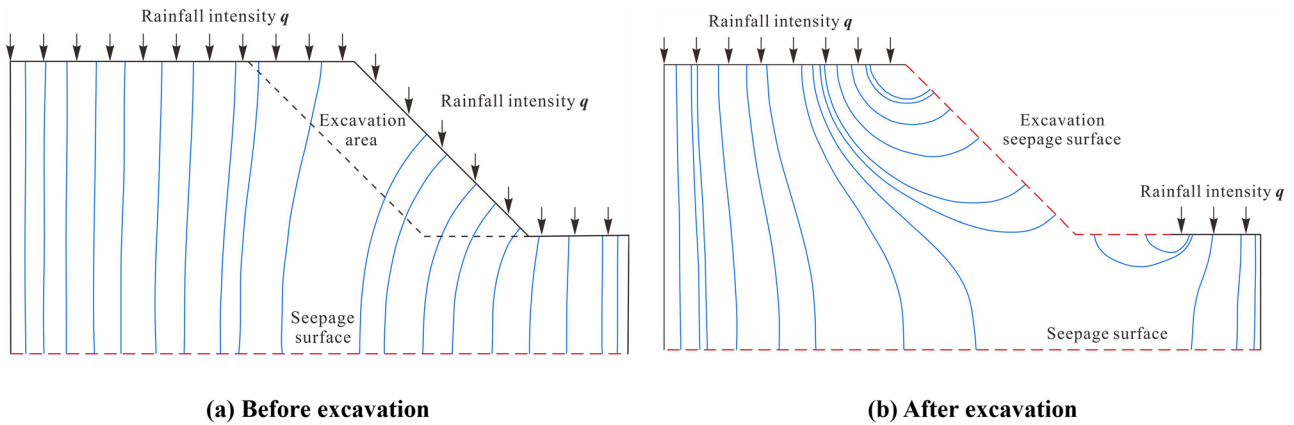


**Fig. 1** Schematic diagram of seepage path changes in unsaturated soil slope excavation simulation (blue lines in the figure are the seepage lines). (a) Before excavation. (b) After excavation

behind the excavation and proceeds slowly over time. For unsaturated slope excavation, finite element simulation calculates the effective stress load of the excavated part, applies the equivalent reaction force to the excavation surface, and combines the effective stress of the remaining soil for analysis (Potts and Zdravkovic 1999). According to Bishop (1959), the effective stress expression of unsaturated soil can be expressed as follows:

$$\sigma' = (\sigma - u_a) + \chi(u_a - u_w) \tag{1}$$

where  $u_a$  is the pore gas pressure,  $u_w$  is the pore water pressure, and  $\chi$  is the effective stress parameter, which can be taken as the saturation state. Excavation is an instantaneous process, and the effective stress of the excavated part can be calculated by pore water pressure of the elements before excavation. However, in the remaining part, the slope seepage caused by excavation is relatively slow. The effective stress of the elements will change due to the variation in the pore water pressure, pore gas pressure, and effective stress

parameter over time. Hence, the element strengths cannot be calculated since the effective stress is uncertain, which makes unsaturated slope excavation simulation difficult.

### Numerical calculation method of stress-seepage fields

The change in the seepage field lags behind that in the stress field, which complicates the numerical calculation. However, in actual engineering, rainfall can only infiltrate into the shallow layers of slopes (Zhang et al. 2020). Pore water can completely dissipate within a few days under sun and wind exposure. If the residual pore water pressure dissipates before excavation, the slope can be restored to its natural state, and the stress of the elements that will be excavated can be determined. Therefore, the method of separate simulation and superposition analysis is proposed to analyse the slope stability under alternating excavation and rainfall. The detailed calculation process is shown in Fig. 2. The specific steps are as follows:

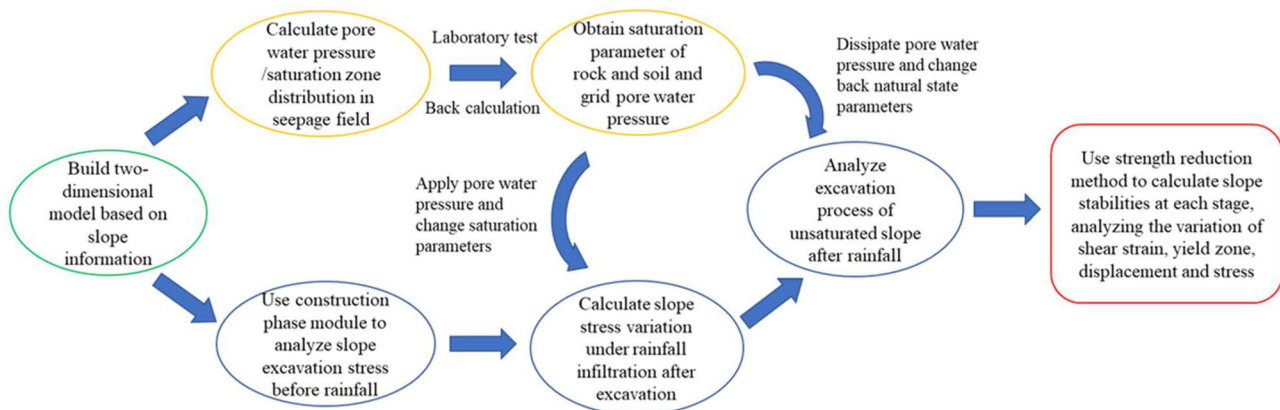


**Fig. 2** Slope stability simulation process under alternating excavation and rainfall

1. The saturated–unsaturated seepage theory is adopted to analyse the slope seepage fields under rainfall conditions during the excavation process. Rainfall intensity is applied to the boundary to obtain the pore water pressure and transient saturation zone distribution of final seepage result under different rainfall events.
2. The saturated mechanical parameters are obtained by physical testing and parameter inversion. The parameters are recorded for the next analysis.
3. For the construction stage, the strength reduction method is used to analyse the stress, deformation, and stability of the slope during excavation before rainfall. In the rainfall stage, referring to the slope final seepage result, the pore water pressure due to the corresponding rainfall is applied to the homologous elements. The mechanical parameters of the elements in the saturation zone are replaced with the saturation parameters. For materials whose strength can be determined by the Mohr–Coulomb criterion, the shear strength of saturated and unsaturated soil elements can be calculated using the following formulas:

Saturated element :  $\tau' = c' + (\sigma - u_w) \tan \varphi$  (2)

Unsaturated element :  $\tau = c + [(\sigma - u_a) + \chi(u_a - u_w)] \tan \varphi$  (3)

where  $c'$  and  $\varphi'$  and  $c$  and  $\varphi$  are the shear strength indices of the rock and soil in the saturated state and the natural state, respectively,  $\sigma$  is the total element stress after excavation,

and  $u_w$  is the applied pore water pressure. The strength reduction method only needs to reduce the shear strength indices of the elements, through which the slope safety factors under the rainfall conditions after the excavation can be calculated.

4. For the unsaturated slope under rainfall infiltration, the previously applied pore water pressure is removed before the next excavation analysis to simulate the pore water pressure dissipation, and the saturation shear strength parameters are replaced with the natural state shear strength parameters to simulate the shear strength restoration. Since the pore water pressure and transient saturation zone are absent, the strength criterion of the rock and soil mass returns to the normal form:

$$\tau = c + \sigma \tan \varphi \tag{4}$$

In this way, the numerical simulation of slope excavation after rainfall infiltration can be regarded as a general excavation simulation. Thus, the safety factors and deformation characteristics are calculated by combining the excavation equivalent stress load method and the strength reduction method.

This method separates the analysis of the slope excavation stress field and rainfall seepage field, solves the difficulty of addressing the stress uncertainty in unsaturated slope excavation simulation by applying/removing pore water pressure and changing the physical–mechanical parameters, and provides an effective approach for slope stability analysis under alternating excavation and rainfall conditions.

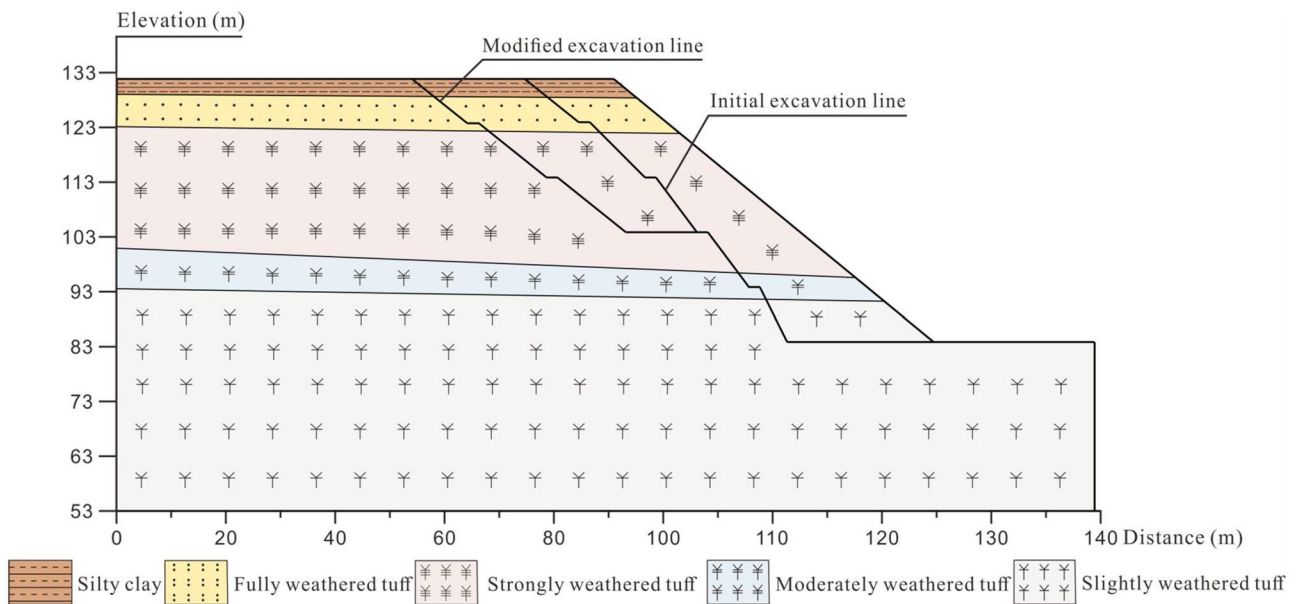


Fig. 3 Slope morphology and engineering geological conditions

**Fig. 4** Status of the slope sliding area in January 2015



## Simulation of alternating excavation and rainfall

To verify the accuracy and effectiveness of the proposed method, a slope with multiple landslides caused by excavation and rainfall is taken as an example. The slope failure process is modelled with the proposed method, the numerical results are compared with on-site monitoring, and the failure mechanism and the effect of instability-inducing factors are further discussed.

## Overview of the highway slope engineering

### Geological survey

The AK2 + 210 ~ AK2 + 610 section slope of a highway reconstruction and expansion project in Guangdong Province, China, is 45 m high with a dip angle of  $262^\circ$  and an unexcavated ratio of 1:1.25. According to the initial design, a five-level excavation with a slope ratio of 1:0.5 ~ 1:1.25, which gradually decreased from low to high, was planned, and the excavation platform was 2 m wide. Since the slope slid several times after the third-level excavation, the design unit proposed a modified excavation plan by adjusting the third- to fifth-level slope ratio to 1:1.25 and increasing the second platform width to 15 m, while the widths of the other platforms were kept to 2 m. The slope is entirely covered by silty clay and fully to strongly weathered tuff. The annual rainfall in this area is 2000 mm and mainly occurs in

summer. The groundwater is bedrock fissure water supplied by atmospheric precipitation. Due to the water absorption properties of the strongly weathered tuff at the upper part of the slope, it is difficult to find groundwater in the study area. The slope morphology and engineering geological conditions are shown in Fig. 3.

### Deformation and failure process and displacement characteristics

#### Slope deformation and failure

This slope exhibits a typical case of deformation and instability induced by rainfall infiltration because the reinforcement and drainage work lagged behind the rapid excavation progress. The slope construction, following the initial design plan, started in November 2014, and the third-level excavation was completed at the end of December 2014. In January 2015, due to heavy rainfall, sliding failures occurred at the lower part of the fourth level to the third-level toe, as shown in Fig. 4. Although construction stopped after the landslide, no treatment measures were applied to the sliding bodies.

After entering the rainy season, the rock and soil masses were softened and deformed due to rainwater infiltration. The top and middle parts of the fourth-level slope were dragged by the sliding bodies, resulting in several tension cracks in the sliding bodies of the third-level slope, as shown in Fig. 5a. Unfortunately, the landslide continued to develop after running through the third- to fourth-level

**Fig. 5** Development of the slope sliding area from May to June 2015



**Fig. 6** Status of the slide after the modified excavation in January 2016



slopes. Similar to the fourth-level slope failure mechanism, the fifth-level slope was dragged and damaged by the lower sliding bodies. Finally, a sliding area that ran through the third- to fifth-level slopes formed in June 2015, as shown in Fig. 5b.

Thus, the design unit proposed a modified excavation plan after the landslide area formed. The construction enterprise cleaned up the landslides in October 2015 and gently excavated the third to fifth level to reach a 1:1.25 slope ratio after completing the excavation of the first and second levels. The second platform was also widened to 15 m, and the excavation was completed at the end of December 2015. During this period, the cracks at the slope did not expand significantly.

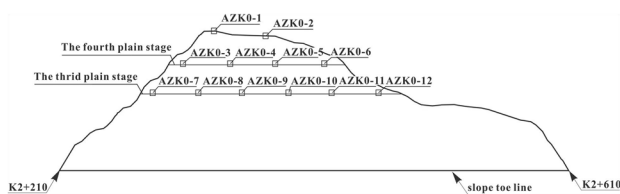
In January 2016, heavy rainfall occurred again in the slope area. At this time, the excavated third- to fifth-level slopes had not yet been supported, and a slide occurred through the third- to fourth-level slopes, as shown in Fig. 6a. Slip surfaces and tension cracks were clearly observed at the toe of the fourth-level slope, as shown in Fig. 6b, and no further slope deformation has occurred since.

Characteristics of excavated slope surface displacements

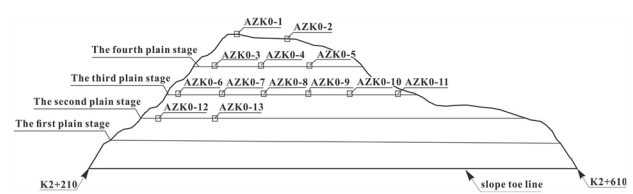
Slope monitoring started in December 2014 and ended in January 2016 due to the deformation and sliding of the excavated slope surface. The levelling measurement method was adopted to monitor the displacement of the third- to

fifth-level slopes during excavation. Considering the disturbance and damage of the monitoring points during the long construction process, the monitoring can be divided into three stages. The layout of the measuring points in each stage is shown in Fig. 7.

Due to a large volume of data, the horizontal displacements of the representative monitoring points at each stage are selected to reflect the deformation, as shown in Fig. 8. The first stage started on December 27, 2014. On January 8, 2015, large local deformation occurred on the third-level slope after excavation, causing a sharp increase in displacement at all the measuring points. From January 15 to 20, heavy rainfall occurred in the slope area, which directly caused third- and fourth-level slope sliding and deformation, resulting in abrupt displacement increases of the third- and fourth-level platforms up to 12.5 mm and 8 mm, respectively. The slope remained stable until the rainy season (April ~ June). The second stage of monitoring started on April 5, 2015, and two new measuring points, AZK0-1 and 0-2, were set up on the slope top to monitor the fifth-level slope deformation. The traction deformation and sliding continued under the action of continuous rainfall, which could be verified by a significant increase in measured displacements on May 25, 2015. On June 19, 2015, a landslide that ran through the third- to fifth-level slopes eventually formed and destroyed almost



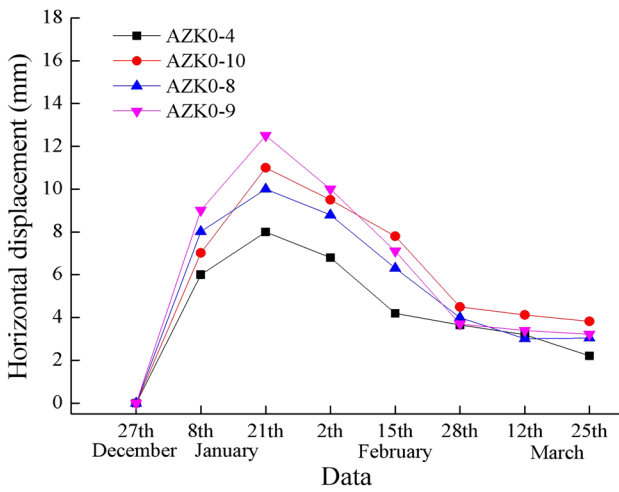
**(a) Schematic diagram of the measuring point layout in the first and second stages**



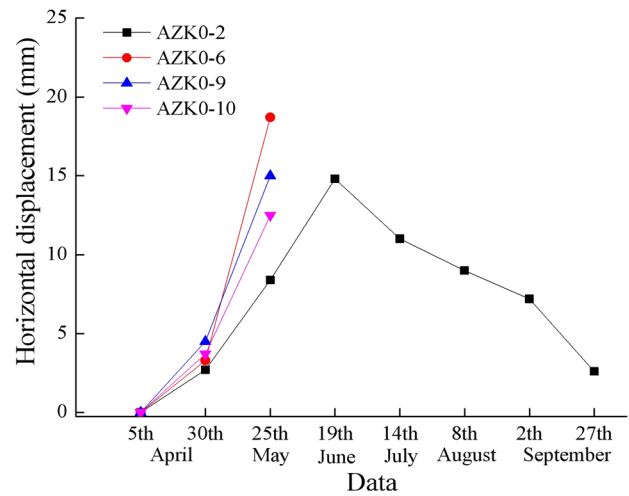
**(b) Schematic diagram of the measuring point layout in the third stage**

**Fig. 7** Schematic diagrams of the measuring point layouts in each monitoring stage (AZK0-1 and 0-2 in the figure are newly added points in the second stage). (a) Schematic diagram of the measuring

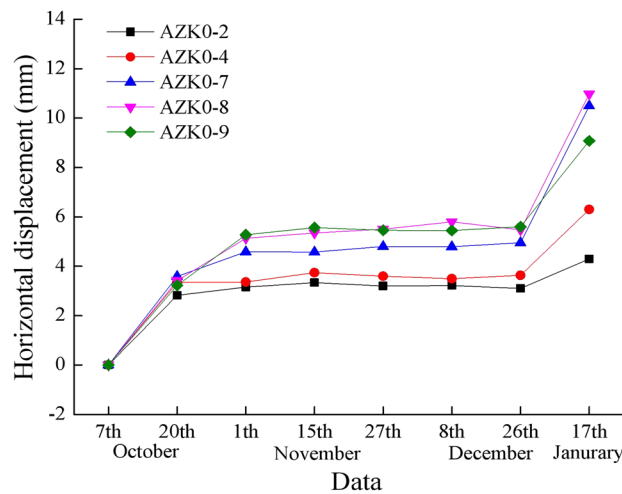
point layout in the first and second stages. (b) Schematic diagram of the measuring point layout in the third stage



(a) The first monitoring stage  
(December 2014 to March 2015)



(b) The second monitoring stage  
(April to September 2015)



(c) The third monitoring stage  
(October 2015 to January 2016)

**Fig. 8** Horizontal displacements of typical measuring points during each stage. (a) The first monitoring stage (December 2014 to March 2015). (b) The second monitoring stage (April to September 2015). (c) The third monitoring stage (October 2015 to January 2016)

all the measuring points except the only one located on the slope top. This left point recorded a maximum displacement of 14.8 mm. The third monitoring stage corresponded to the modified excavation in October 2015. During the excavation period from October 7 to December 26, 2015, the displacements were relatively gentle. However,

on January 17, 2016, rainwater infiltrated the unsupported excavated slope surface and caused the third-level slope to be damaged and deformed once again. Because of this heavy rain, the maximum measured displacement sharply increased to 11 mm, and the fourth-level platform displacement increased to 6.3 mm.

## Stability back analysis, model and parameters

### Stability back analysis and parameter inversion

#### 1. Back analysis of slope stability

According to the deformation and displacement characteristics, the slope experienced two excavation events and several heavy rainfall events, i.e. several excavation and rainfall cycles. Two sliding failures were directly caused by rainfall infiltration after excavation. The failure at the initial excavation stage was affected by intermittent rainfall, which illustrates the progressive failure characteristics. The micro-geomorphological characteristics of the tension cracks and front shear outlets of the two failures are fully developed, but no large-scale deep landslides formed. Wang et al. (2017) summarised the corresponding relationship between the slope deformation characteristics and the safety factors and suggested that the deformation of the cutting slope can be divided into the creeping stage ( $1.05 < F_s < 1.1$ ), the extrusion stage ( $1.02 < F_s < 1.05$ ), the sliding stage ( $0.98 < F_s < 1.02$ ) and the sudden slip stage ( $0.95 < F_s < 0.98$ ). According to their study, it is determined that the two sliding failures are in the sliding stage with a safety factor of  $0.98 \sim 1.02$ . Since rainfall directly causes slope failure, it can be considered that the soil in the shallow failure area is saturated, so its shear strength parameters need to be obtained. In the absence of field test conditions, the inversion of the soil saturation strength parameters can be carried out according to the safety factor range combined with the drilling exploration results. The inverse strength parameters can be brought into the subsequent finite element simulation. If the simulated deformation characteristics are in good agreement with the field monitoring results, the effectiveness of the stability back analysis will be validated.

#### 2. Inversion of shear strength parameters

The inverse calculation of the slope shear strength parameters is based on the limit equilibrium method (Nguyen 1984; Ishii et al. 2012; Shinoda et al. 2019). By assuming that the slope is in the critical state, the bal-

anced relationship between the sliding and anti-sliding forces on the corresponding sliding surface will be used to back-calculate the soil shear strength indices. This paper applies GeoStudio software to perform parameter inversion based on the limit equilibrium method using the slope/W module. The Spencer method of stability analysis and the sliding surface optimization option are adopted, and the entry and exit of the sliding surface are set according to the field failure characteristics. Meanwhile, the safety factor range ( $0.98 < F_s < 1.02$ ) is used as the inversion target, and the saturation density and shear strength parameters determined during the geological survey are used as the initial values. When the calculated critical sliding surface position and safety factor are consistent with the field observation, the calculation is stopped and the shear strength parameters are record. Because local sliding failure occurred after the excavation plan was modified, the slope section at the initial excavation stage was selected to conduct the parameter inversion of the third- to fifth-level shallow landslide. According to the drilling exploration results, the rock and soil physical and mechanical parameters are listed in Table 1. The weights in parentheses are the saturation weights.

Since the third- to fifth-level sliding areas contain silty clay and fully to strongly weathered tuff layers, the saturated shear strength parameters of the silty clay should be determined first, and the parameters of the tuff layers need to be reduced by a certain proportion. Referring to the results of experimental studies on the saturated shear strength of silty clay (Yang et al. 2016; Jotisankasa et al. 2009; Liu et al. 2020), the saturated cohesion force and internal friction angle of silty clay are assumed to be 10 kPa and  $13^\circ$ , respectively. Considering that the saturated shear strength of the two tuff layers should be consistent with the degree of weathering and that the cohesive force and internal friction angle should maintain a certain proportional relationship after reduction, a uniform proportional coefficient is used to reduce the shear strength parameters of the tuff layers simultaneously. According to

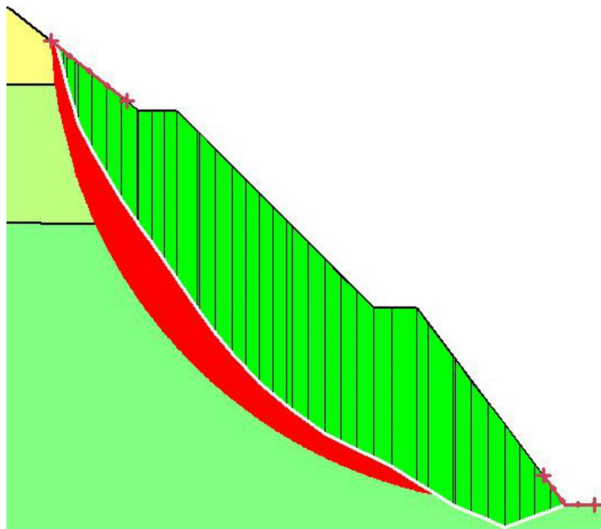
**Table 1** Physical and mechanical parameters of the rock and soil

Types of rock and soil layers	Deformation modulus (kPa)	Poisson's ratio	Weight (kN/m <sup>3</sup> )	Cohesive force <i>C</i> (kPa)	Internal friction angle $\varphi$ (°)
Silty clay	$3 \times 10^4$	0.28	20 (21.5)	15	15
Fully weathered tuff	$1.3 \times 10^5$	0.31	21 (22.5)	29.4	19
Strongly weathered tuff	$6.1 \times 10^5$	0.27	22 (23.5)	37	24
Moderately weathered tuff	$8.3 \times 10^5$	0.29	23.5 (24)	70	29
Slightly weathered tuff	$1.7 \times 10^6$	0.22	24.5 (24.8)	90	31



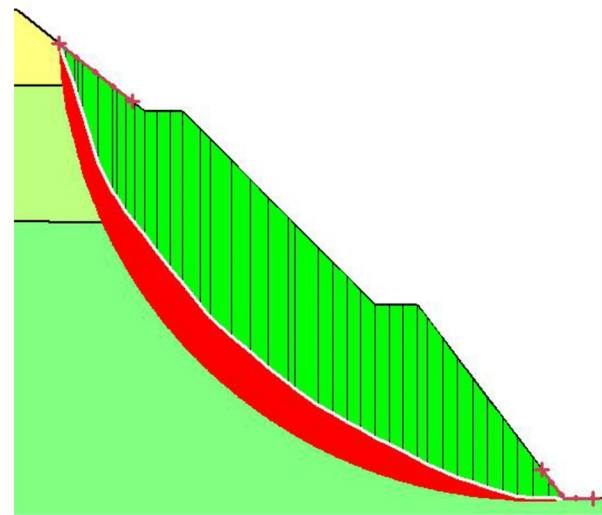
the direct shear test results of the tuff in the moisture absorption process (Tang et al. 2015; Zuo et al. 2016), both the cohesive force and internal friction angle can be reduced by the water action, and the reduction rate of the former is several times higher than that of the latter. In this study, the reduction ratio between the two

indices is set to 3:1, 4:1, and 5:1 for inversion, and the dichotomy concept is applied to make the calculated safety factor approach the inversion target range. The final sliding surfaces obtained by the inversion analysis are shown in Fig. 9, and the inverse saturation parameters are listed in Table 2.



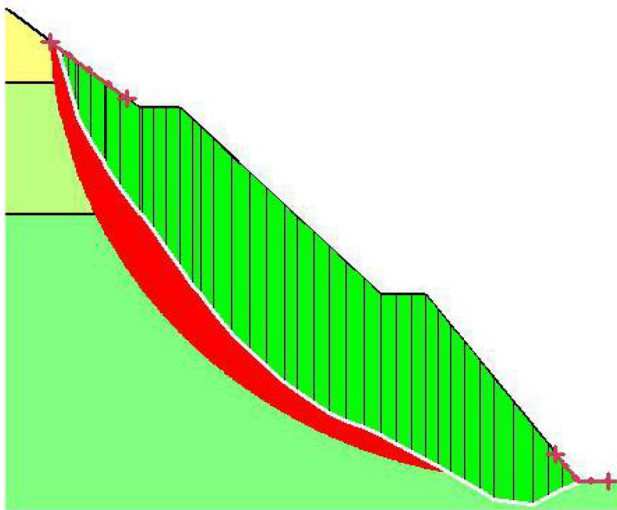
(a) The reduction ratio of 3:1

( $F_s=0.998$ )



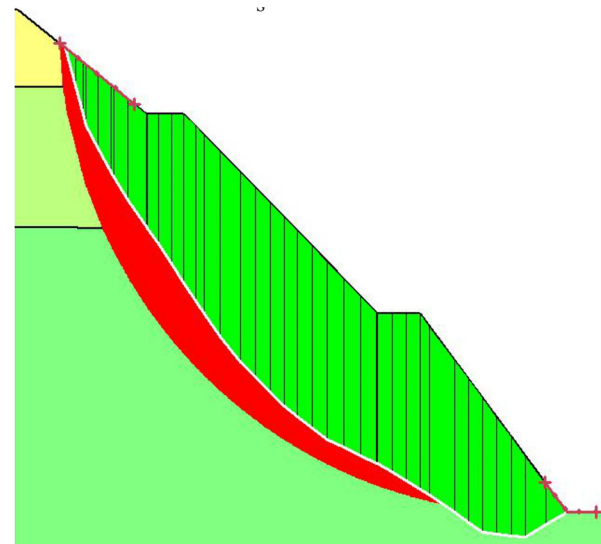
(b) The reduction ratio of 4:1

( $F_s=0.982$ )



(c) The reduction ratio of 4:1

( $F_s=0.994$ )



(d) The reduction ratio of 5:1

( $F_s=0.996$ )

**Fig. 9** Final sliding surfaces obtained by the inversion analysis. (a) The reduction ratio of 3:1 ( $F_s=0.998$ ). (b) The reduction ratio of 4:1 ( $F_s=0.982$ ). (c) The reduction ratio of 4:1 ( $F_s=0.994$ ). (d) The reduction ratio of 5:1 ( $F_s=0.996$ )

**Table 2** Inversion of tuff saturation parameters

Reduction ratio between $C$ and $\varphi$	Fully weathered tuff		Strongly weathered tuff		Safety factor
	$C$ (kPa)	$\varphi$ (°)	$C$ (kPa)	$\varphi$ (°)	
Initial parameters	29.40	19	37	24	1.236
3:1	26.40	18	34	23	1.155
	23.40	17	31	22	1.076
	20.40	16	28	21	0.998
	19.7	15.75	27.25	20.75	0.978
4:1	19	15.50	26.50	20.50	0.944
	25.4	18	33	23	1.139
	21.4	17	29	22	1.044
	17.4	16	25	21	0.938
	19.4	16.75	27	21.75	0.994
5:1	18.4	16.50	26	21.50	0.982
	24.40	18	32	23	1.081
	19.40	17	27	22	0.996
	14.40	16	22	21	0.909
	16.9	16.50	24.50	21.50	0.971

Table 2 shows that the safety factors calculated by the partial saturation parameters under the three tested ratios reached the inversion target. Two sets of saturation parameters under a reduction ratio of 4:1 meet the inversion target, with safety factors of 0.982 and 0.994. For the reduction ratios of 3:1 and 5:1, each condition has a set of saturation parameters satisfying the inversion target with safety factors of 0.998 and 0.996, respectively. However, based on Fig. 9 and the final sliding surfaces obtained, except for the result with a safety factor of 0.982, the other inversed critical sliding surfaces near the shear outlet are inconsistent with the on-site situation. Thus, the set of saturation parameters with the highest safety factor of 0.982 under the ratio of 4:1 are selected for subsequent numerical calculations, i.e., the fully weathered tuff parameters are  $C = 18.4$  kPa and  $\varphi = 16.5^\circ$ , and the strongly weathered tuff parameters are  $C = 26$  kPa and  $\varphi = 21.5^\circ$ .

### Model establishment and calculation conditions

Based on the engineering geological section shown in Fig. 3, Midas-GTX software is used to establish a two-dimensional finite element model. Vertical sliding bearings are applied to the left and right boundaries, while fixed bearings are applied to the bottom boundary. The slope safety factor is calculated by the strength reduction method. Because the slope simulation is complicated under alternating excavation and rainfall conditions, the proposed method is used to simulate the excavation stress field and the rainfall seepage field separately. Then, the seepage field results are applied to the corresponding

**Table 3** Simulated rainfall conditions

Rainfall conditions	Accumulated rainfall (days)
First rainfall	75 mm (5)
Second rainfall	979.5 mm (42)
Modified excavation rainfall	412.5 mm (17)

rainfall stages during the excavation stress analysis. The steps of the seepage and excavation analysis are as follows:

#### 1. Seepage analysis conditions and permeability coefficient

The Midas-GTX transient seepage module simulates the rainfall process. The analysis time step is one day. The daily flow during the rainfall period is converted to the seepage boundary functions and applied as the flow boundary conditions. Because no groundwater is found, the initial groundwater level is set in the slightly weathered tuff layer to meet the transient seepage analysis conditions without affecting the analysis results. Meanwhile, for the convenience of analysis, the three rainfall periods of January 2015, May–June 2015, and January 2016 are simplified into three heavy rainfall events. The first two are called the first and second rainfall, respectively, and the later one is called the modified excavation rainfall. According to the meteorological data, the intensity and duration of rainfalls are shown in Table 3 with the seepage boundary functions displayed in Fig. 10.

The unsaturated soil permeability coefficient function is calculated using the soil–water characteristic curve and the saturated permeability coefficient (Fredlund 1998). The Van Genuchten model (Bishop and Blight et al. 1963) is applied to determine the former. The governing equation of the water content model is shown as follows:

$$\theta_w = \theta_r + \frac{\theta_s - \theta_r}{\left[1 + \left(\frac{\psi}{a}\right)^n\right]^m} \quad (5)$$

where  $\theta_w$  is the volumetric water content,  $\theta_r$  is the residual volumetric water content,  $\theta_s$  is the saturated volumetric water content,  $\psi$  is the negative pore water pressure,  $a$ ,  $n$ , and  $m$  are the curve fitting parameters.

Because the moderately to slightly weathered layer is relatively deep and has little effect on the slope stability, its permeability characteristics are not considered. According to geological survey data and previous research results (Zhao et al. 2017; Tan et al. 2018), the parameters of the Van Genuchten model and the saturated permeability coefficients  $K_s$  of silty clay, fully to strongly weathered tuff layers are listed in Table 4. Simultaneously, the unsaturated soil permeability function curves and water content function curves are shown in Figs. 11, 12, 13, 14, 15, and 16.

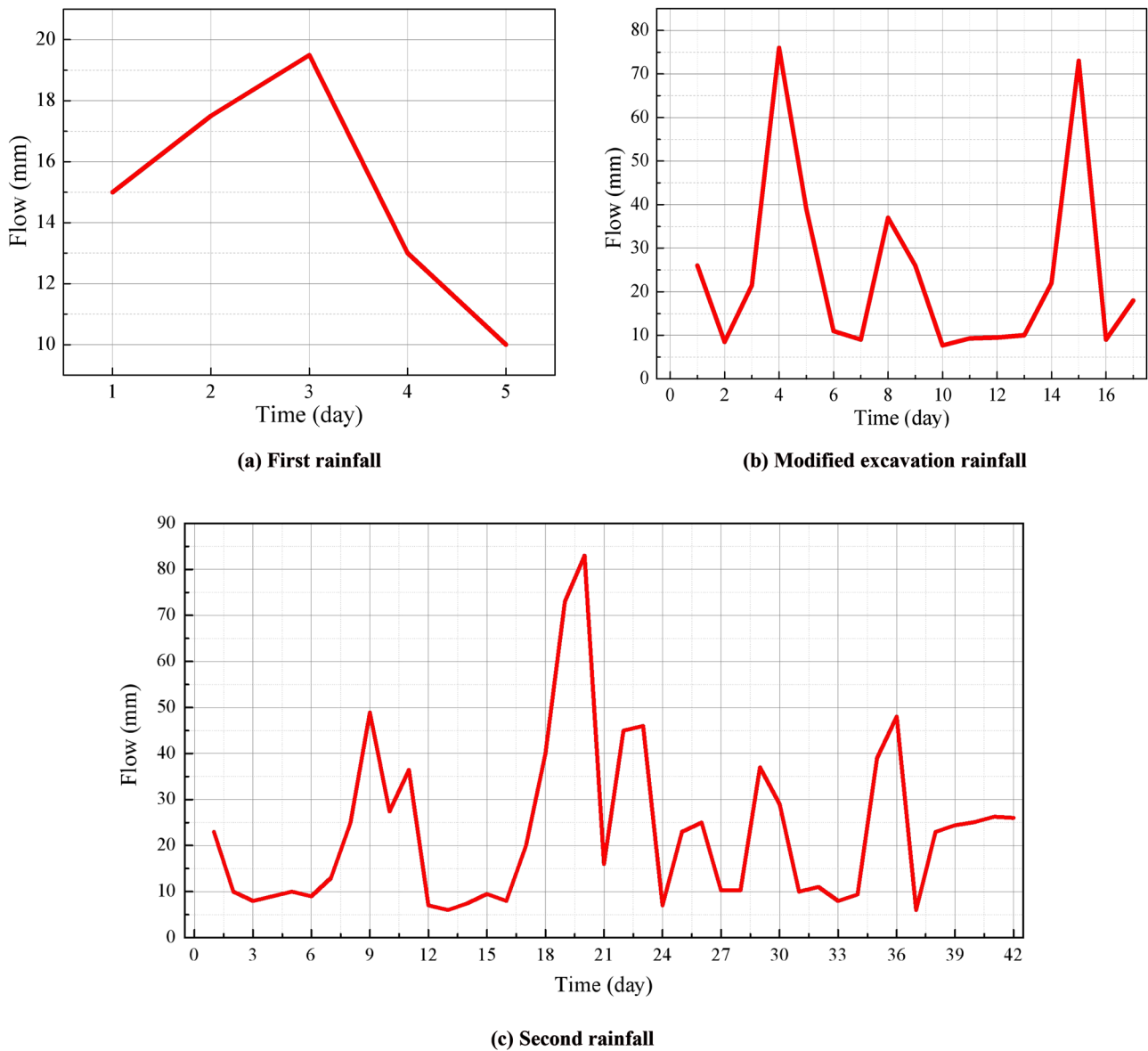


**Fig. 10** The seepage boundary functions of the three rainfall events. (a) First rainfall. (b) Modified excavation rainfall. (c) Second rainfall

2. Excavation analysis conditions

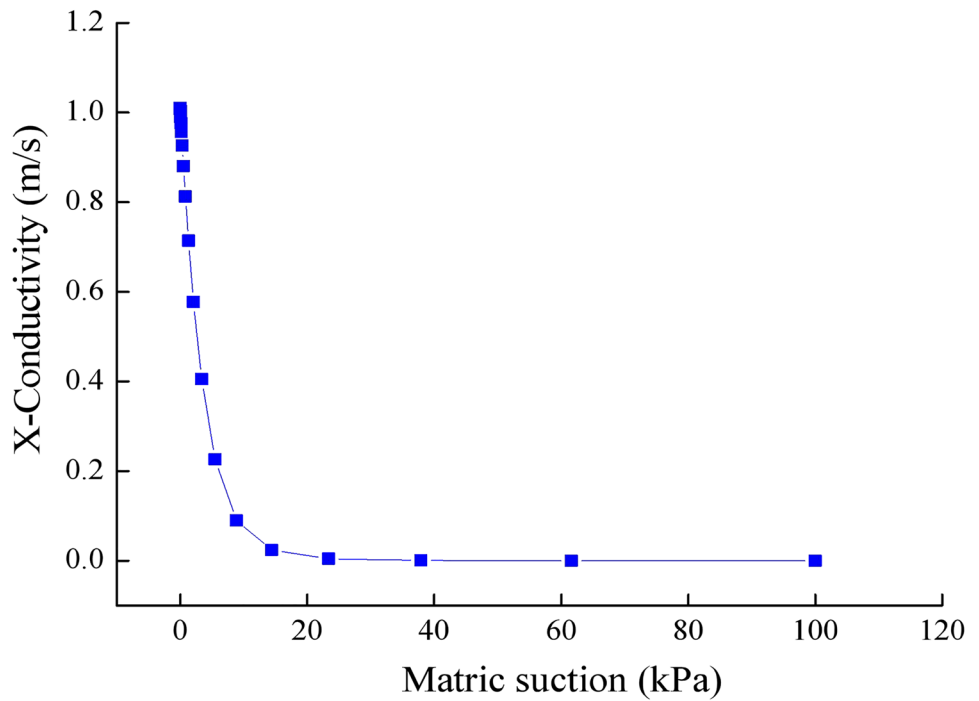
The sequence of initial excavation first and modified excavation second is adopted in the simulation. The initial excavation construction sequence is fifth-level slope excavation → fourth-level excavation → third-level excavation → first rainfall → second rainfall → fifth-level modified and lower two-level initial excavation → fourth-level modified excavation → third-level modified excavation

→ modified excavation rainfall. In the rainfall stage, based on the final seepage results of the three rainfall events, the element property modification and boundary import functions of the Midas software are used. Clearly, the shear strength parameters of the elements in the transient saturation zone are modified, and pore water pressure is applied to the elements. These two changes form the new computation conditions. Com-

**Table 4** Van Genuchten model parameters and saturated permeability coefficients

Types of rock and soil layers	$a$ (kPa)	$n$	$m$	$\theta_r$	$\theta_s$	$K_s$ (m/s)
Silty clay	10	1.9	0.47368	0.04	0.28	$1.17 \times 10^{-5}$
Fully weathered tuff	3.56	1.44	0.30556	0.20	0.44	$1.63 \times 10^{-7}$
Strongly weathered tuff	4.29	1.46	0.31506	0.19	0.45	$1.47 \times 10^{-7}$

**Fig. 11** Permeability function curve of the silty clay



combined with the Midas activation/passivation function, the new computation conditions are activated during the rainfall phase and passivated in the next phase, to simulate the rainfall infiltration/dissipation effect.

**Analysis of slope simulation results**

**Analysis of slope seepage results**

Considering the durations of the three rainfall events are different, to make clear the influence of rainwater infiltration on slope stress, the rainfall process is divided into

three stages in the chronological order for each rainfall event, i.e. early stage, middle stage, and final stage. The contour maps of pore water pressure induced by the first, second, and modified excavation rainfall seepage are shown in Fig. 17, in which the white dotted lines are the infiltration lines and the soil above them is saturated.

Figure 17 shows the distribution changes of pore water pressure in the early, middle, and final (rainfall end) stages of the three rainfall events. In the early stage, since the rainfall intensity is far less than the permeability coefficient of the rock and soil, the slope is unsaturated, and the pore water pressure is all negative. In the middle stage, the rainfall intensity exceeds the saturated permeability coefficient

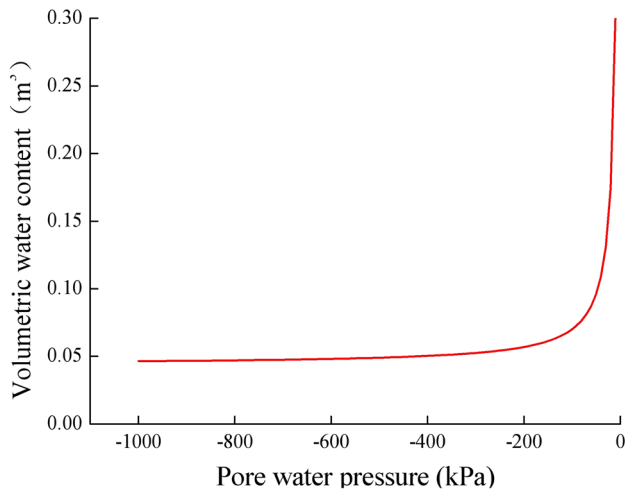


**Fig. 12** Water content function curve of the silty clay

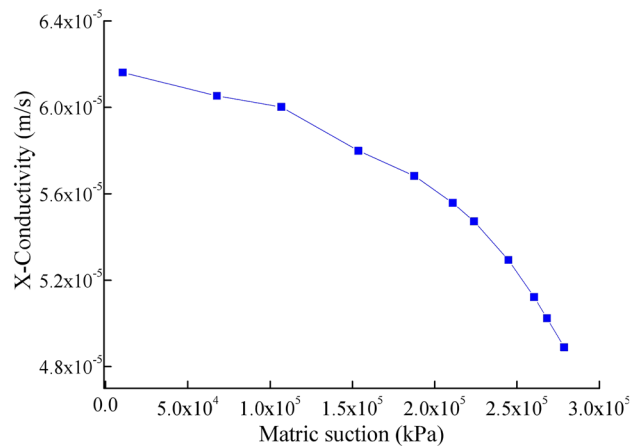


**Fig. 13** Permeability function curve of the fully weathered tuff

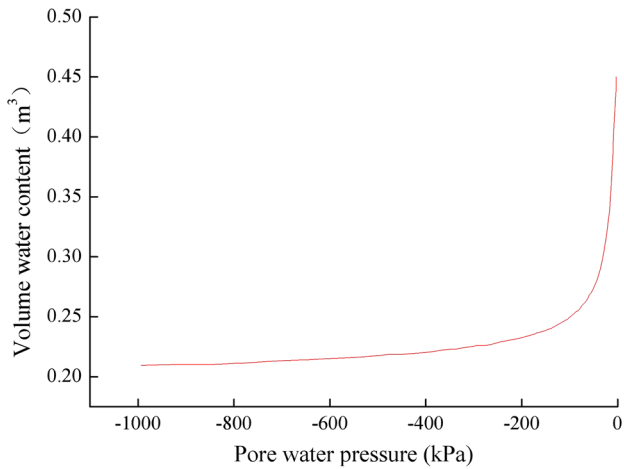


Fig. 14 Water content function curve of the fully weathered tuff

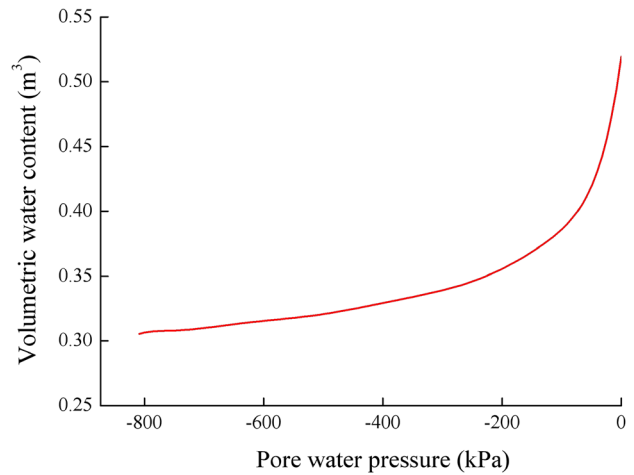


Fig. 16 Water content function curve of the strongly weathered tuff

of tuffs, the matrix suction of the rock and soil underneath slope surface gradually loses, and the pore water pressure turns from negative to positive. Transient saturation zone appears near the slope surface because of the second and modified excavation rainfall events. In the final stage, the rainfall intensity is much higher than the permeability coefficient of the tuff layers, and it even exceeds the silty clay's permeability coefficient during the second rainfall event. The transient saturation zone expands to varying extents. Influenced by the different permeability coefficients, the transient saturation zone near the excavated slope surface is much larger than the top, which also explains why the

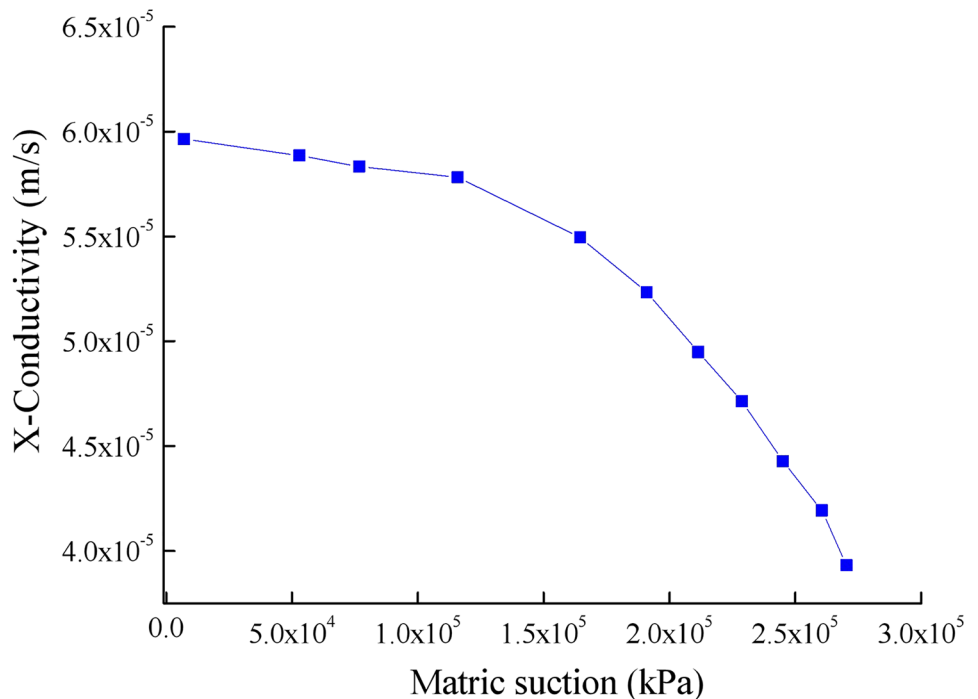
landslides often occur at the excavated surface. The pore water pressure values basically show a trend of first decreasing and then increasing with buried depth, and the extreme value appears inside the slope, which is consistent with the previous research results (Qiu et al. 2020; Jiang et al. 2015).

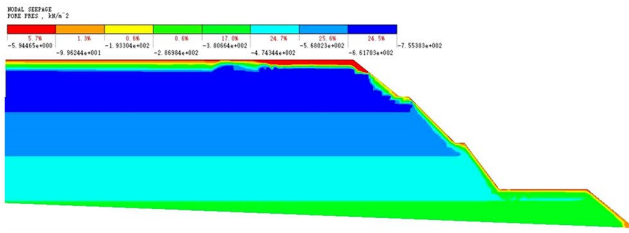
**Deformation and failure process analysis**

**Excavation deformation process and slope stability**

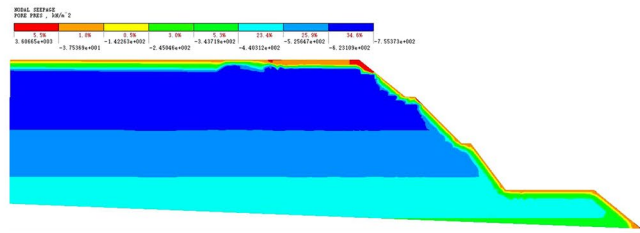
Combining the simulated results and the monitored field deformation results, the distribution of the maximum shear

Fig. 15 Permeability function curve of the strongly weathered tuff

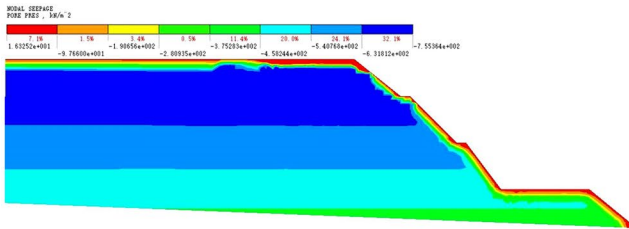




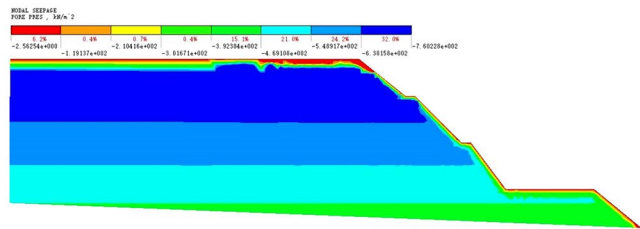
(a) First rainfall (day 1)



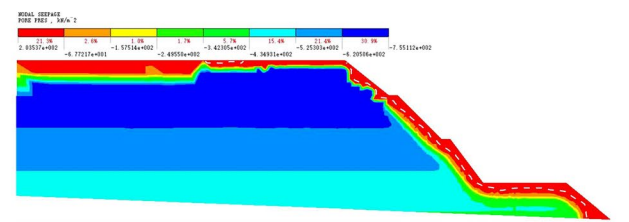
(b) First rainfall (day 3)



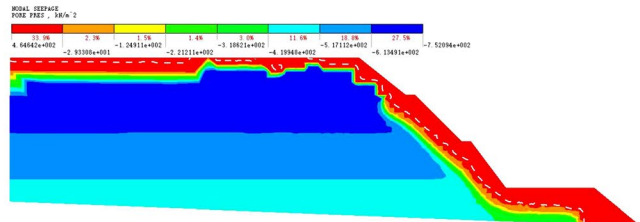
(c) First rainfall (day 5)



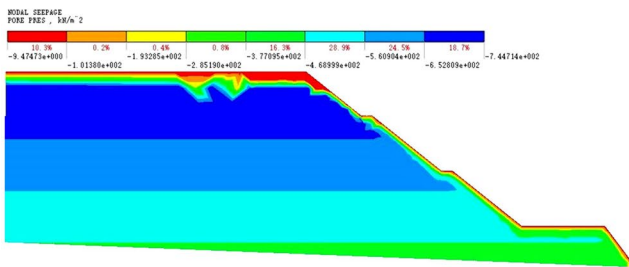
(d) Second rainfall (day 1)



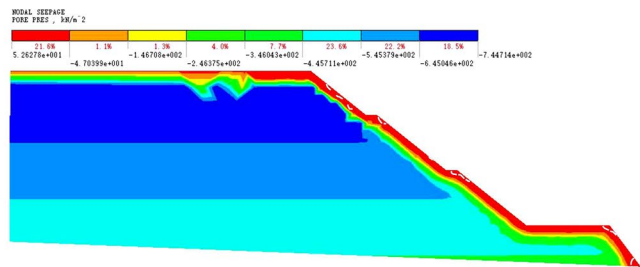
(e) Second rainfall (day 21)



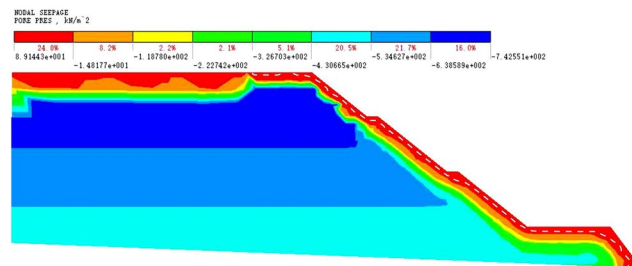
(f) Second rainfall (day 42)



(g) Modified excavation rainfall (day 1)



(h) Modified excavation rainfall (day 9)



(i) Modified excavation rainfall (day 17)

**Fig. 17** Pore water pressure distribution with time induced by three rainfall events. (a) First rainfall (day 1). (b) First rainfall (day 3). (c) First rainfall (day 5). (d) Second rainfall (day 1). (e) Second rainfall

(day 21). (f) Second rainfall (day 42). (g) Modified excavation rainfall (day 1). (h) Modified excavation rainfall (day 9). (i) Modified excavation rainfall (day 17)

strains of the third- to fifth-level slopes and the evolution of the slope body yield state during the excavation are shown in Fig. 18. Meanwhile, “the fifth-level modified excavation and lower two-level initial excavation” will be abbreviated as “the fifth-level and lower part excavation” for convenience in the following description.

During the initial excavation stage, a small amount of unloading deformation appears near the slope surface in the early period. As the excavation volume increases, the high stress concentrates at the toe of the excavated surface, where the shear plastic zone forms and extends to the inner slope. Moreover, some elements on both sides of the plastic zone undergo tensile yielding. After rainfall, the shear plastic zone quickly expands to the slope top, and the area of tensile yield elements gradually extends upwards from the third-level slope. Eventually, the two areas extend through the entire excavated slope. During the modified excavation stage, the early grading excavation causes a shallow shear

plastic zone to form, and the later rainfall induces plastic zone expansion. A high stress concentration appears in the second platform, while tensile failure mainly occurs in the formed third level slope.

Figure 19 shows the slope stability in each excavation stage. The slope stability first decreases with the excavation process, then slowly rises, and finally decreases rapidly. The safety factors are 1.02, 0.98, and 1.02 for the first, second, and modified excavation rainfall stages, respectively. Considering the parameter inversion calculation result (0.982), the four safety factors are all in the target safety factor range of the stability back analysis, and the safety factors and sliding surfaces of the second rainfall stage and inversion result almost coincide, which demonstrates that the numerical simulation and the inversion analysis have good consistency. According to the slope excavation sequence, the deformation characteristics will be analysed separately in the two excavation stages.

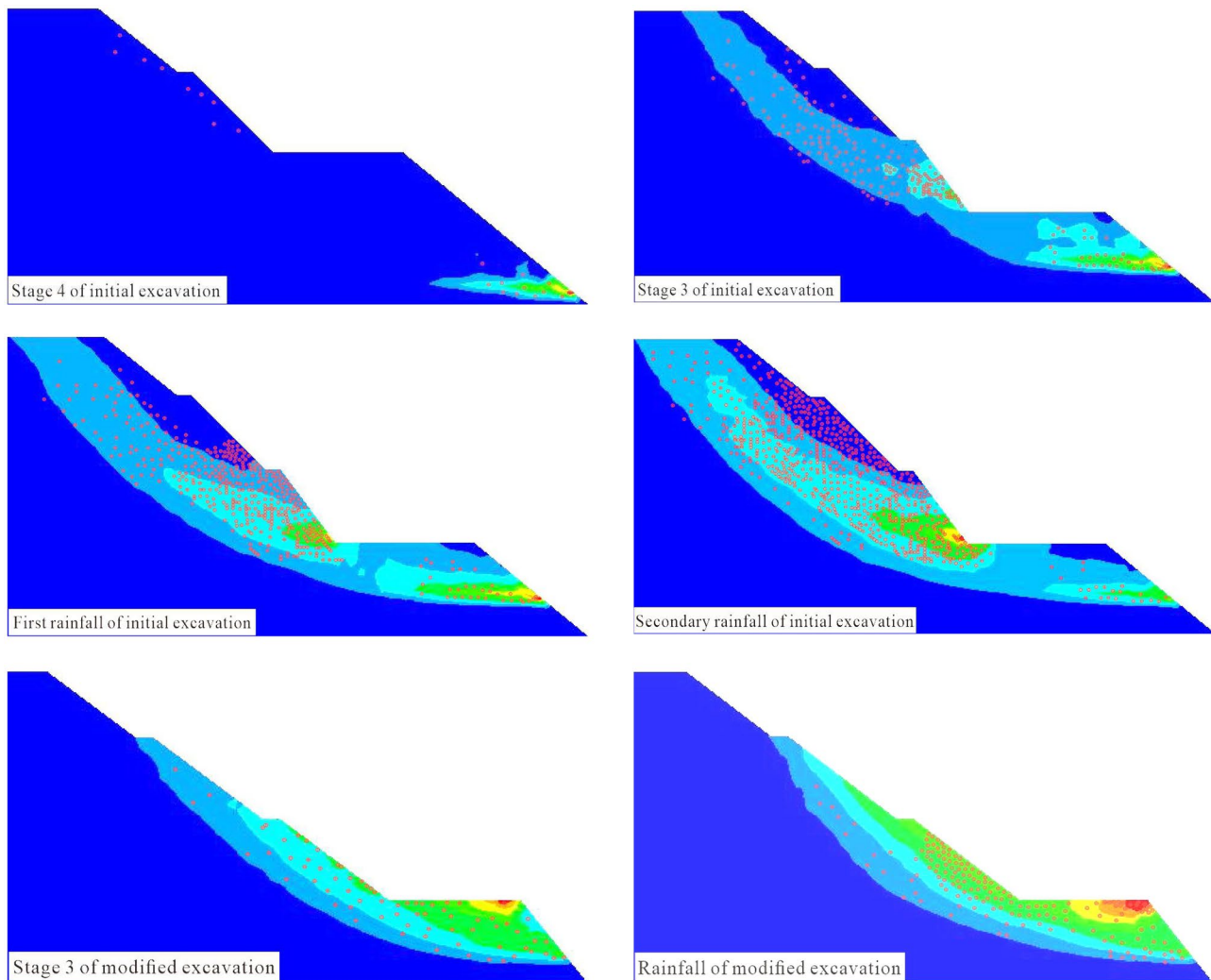


**Fig. 18** Maximum shear strain and yield evolution in the slope (red dots in the figures represent tensile yield elements)

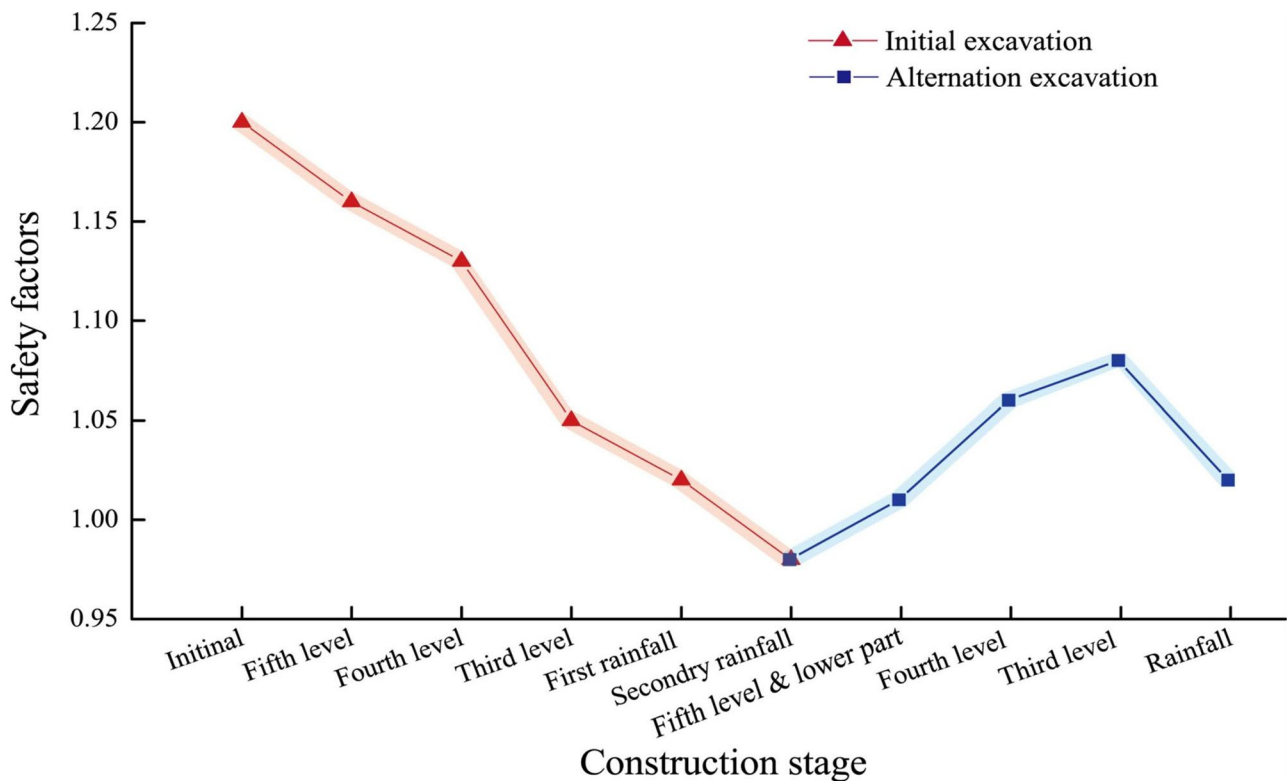


Fig. 19 Safety factor in each stage of the slope excavation sequence

### Characteristics of initial excavation stage

The slope stability gradually decreases as the initial excavation progresses. Before the third-level excavation, the slope is in an unloading and rebounding state. Excavation has a small effect on the slope stress, and only a few tensile yield elements appear near the formed surface. After the third-level excavation, the slope enters a shear fracture state, with the safety factor dropping to 1.05, and large local deformation occurs. The maximum horizontal displacement of the initial third-level slope excavation is 8.02 mm, as shown in Fig. 20. Continuous excavation disrupts the slope stress balance and triggers a high stress concentration to form at the excavated toe and subsequent shear slip. Then, the damaged toe drags the upper part of the slope to form the tensile stress zone, as shown in Fig. 21. This area is basically consistent with the maximum shear strain area, indicating that sliding failure is mainly caused by the pulling and stretching of the lower parts and shows the characteristics of typical tensile-shear failure. The slope deformation exhibits an overall sliding trend after the third-level excavation.

The on-site observations after the first rainfall event are shown in Fig. 4, and the slope safety factor is reduced from 1.05 to 1.02. The infiltration of rainwater produces a transient saturated zone in the shallow layers, as shown in Fig. 17. The shear strength and density of the rock and soil

mass in the saturation zone decreases and increases rapidly, respectively. The elements that undergo tensile yielding are mainly located in the middle and lower parts of the fourth-level slope. The internal shear yield zone expands, indicating that the tensile-shear failure area extends upwards from the third-level slope. The fourth-level slope is dragged to deform by the lower parts, and the slope approaches the limit equilibrium state. After the second rainfall, the slope failed ( $F_s < 1.0$ ), and the transient saturated zone expands to the inner slope, as shown in Fig. 18. The tensile-shear failure area covers the entire excavated slope level, and a shallow landslide that runs through the third- to fifth-level slopes finally forms, as shown in Fig. 22.

### Characteristics of the modified excavation stage

Before the modified excavation, the long-term quiescence caused the shallow saturated soil to return to its natural state: the pore water pressure completely dissipated. The third- to fifth-level modified excavation removed the front sliding bodies, which reduced the slope stress level, and the gentle excavation slope ratio stabilised the upper weathered tuff. The modified excavation led to a slow growth of the slope safety factor. The simulation results indicate that the safety factor rises to 1.06 after the third-level excavation, and the slope is basically stable. Although the excavation causes a few elements



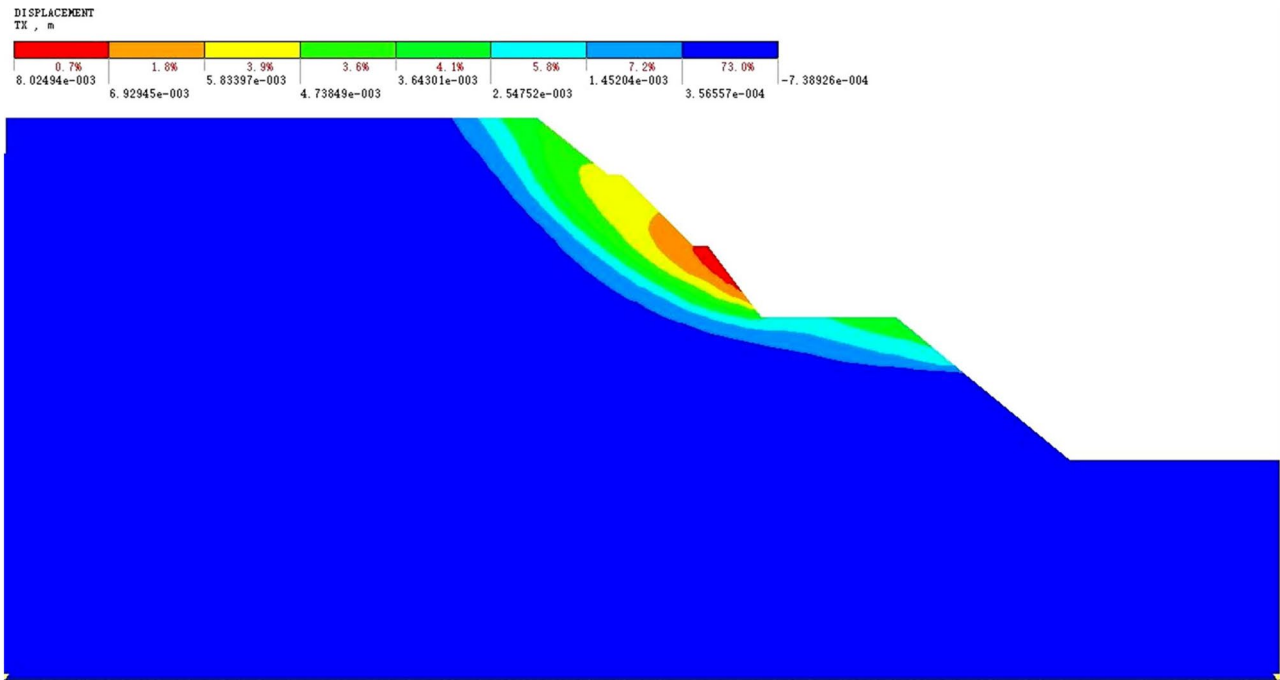


Fig. 20 Horizontal displacement distribution after initial excavation of the third-level slope

under tension to yield, the slope is unable to greatly deform and slide due to the low stress level. After rainfall, the infiltration rainwater produces a saturated zone again, as shown in Fig. 17. The pore water pressure and the soil’s additional bulk density cause the slope stress level to rise again, and the shear

strength is also reduced due to the water softening effect. The toe of the excavated third-level slope is unstable and undergoes further damage, which pulls the middle and upper bodies to form slip through the third and fourth-level slopes, as shown in Fig. 23. The maximum horizontal displacement of the slope

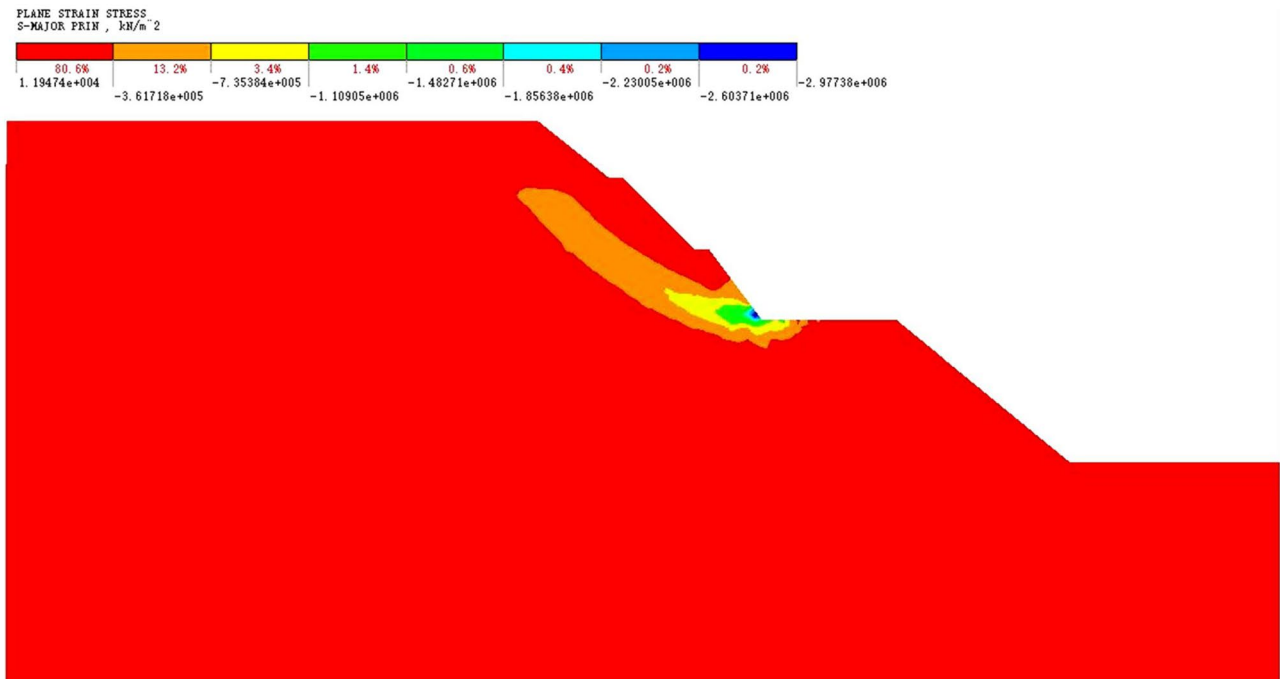


Fig. 21 Maximum principal stress distribution after initial excavation of the third-level slope

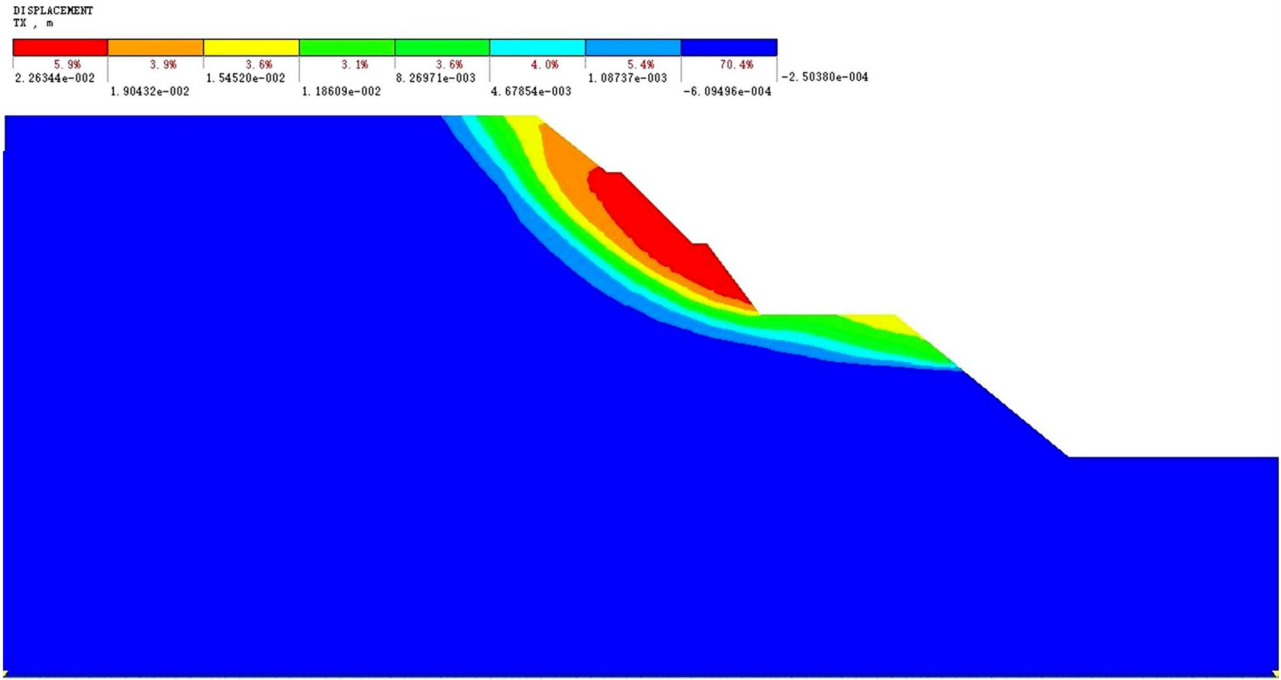


Fig. 22 Horizontal displacement distribution after the second rainfall

is 10.5 mm, close to the 11 mm maximum horizontal displacement measured at the third platform monitoring point. The simulated deformation range is very similar to the actual sliding failure area, and the simulation is also in good agreement

with the inversion analysis, which further indicates that the numerical simulation accurately reveals the deformation and failure process. Thus, the validity and accuracy of the proposed analysis method is fully verified.

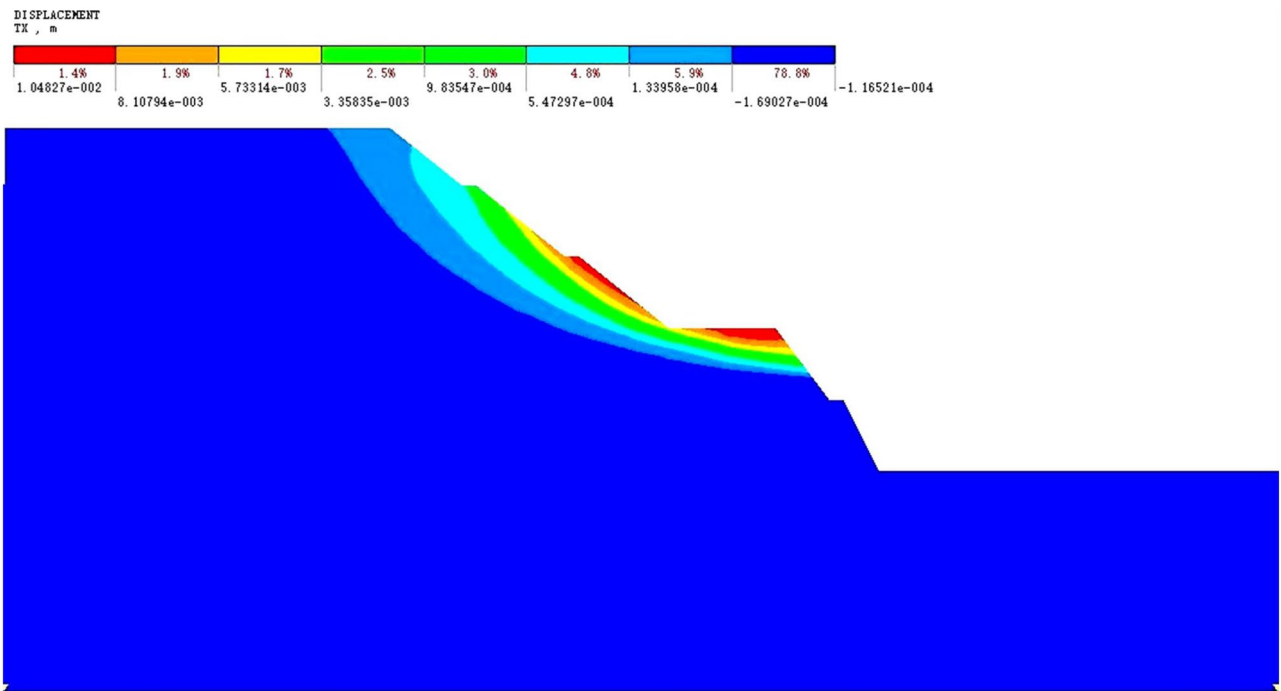


Fig. 23 Horizontal displacement distribution after the modified excavation rainfall

## Analysis of inducing factors and instability mechanism

Since the simulation accurately reproduces the slope deformation and failure process, the inducing factors and failure mechanism of slope instability can be discussed based on the simulation results. In the following, the inducing effects of excavation and rainfall will be analysed separately, and then the slope instability mechanism will be further discussed.

The excavation effect on the slope is reflected by two aspects: (1) the unloading effect of excavation triggers stress adjustment and (2) the excavated bare surface provides natural infiltration channels for rainwater. Regarding the former aspect, the unloading effect has a totally different impact on the slope as the excavation slope ratio changes. During the initial excavation stage, the third-level excavation resulted in a high stress concentration at the excavated toe, exposure of the potential weak zone and tensile yielding of slope bodies, which resulted in tensile failure of the toe. The upper slope therefore lost its mechanical support. The unloading effect produced by rapid excavation is the main reason for the slope instability during the initial stage. During the modified excavation stage, the excavation unloading reduced the stress level and improved the slope stability due to the gentle excavation slope ratio. However, the excavation destroyed the original slope protection. Without the implementation of waterproofing measures during the excavation, the excavated bare surface was exposed for a long time, which allowed rainwater infiltration and indirectly caused slope failure during the modified excavation stage.

Rainfall has a negative effect on the excavated slope stability. Rainwater infiltrated along the bare slope surface and directly caused two sliding failures. The effect is also reflected in two aspects: (1) the pore water pressure changes the slope stress state and (2) the transient saturated zone reduces the shear strength of the rock and soil mass. During the first and second rainfalls, the surge of pore water pressure caused the slope stress to redistribute and the effective soil stress to decrease, with the soil bulk density increasing and the shear strength decreasing in the transient saturated zone, which resulted in the decrease in slope stability, connection of shear plastic zones and concentration of tension yielding in the excavated slope areas. The slope showed progressive failure characteristics with increasing rainfall intensity. The rainwater produced a saturated zone at the modified excavation rainfall stage, which caused local damage to the slope that had already been stabilised. Rainwater infiltration was the main reason for the slope instability during the modified excavation stage.

The slope instability mechanism determined from the analysis of the above factors is as follows: During the initial excavation stage, due to the rapid excavation disturbance, the slope stress was redistributed, and the potential weak zone was fully exposed, which resulted in large local deformation

of the excavated slope areas and weak zone expansion along with the loosening of the rock and soil. During the modified excavation stage, the gentle excavation slope ratio reduced the slope stress level, and the exposed bare surface created favourable conditions for rainwater infiltration. Rainfall sharply increased the slope stress level, resulted in sliding surface expansion and finally caused large local deformation and failure.

## Conclusions and suggestions

This research focuses on understanding the slope deformation characteristics and instability mechanism under alternating excavation and rainfall conditions. The AK2 + 210 ~ AK2 + 610 section slope of a highway in Guangdong Province, China, is studied using a proposed method. The slope failure process, inducing influencing factors, and instability mechanism are analysed in detail, and the key findings are summarised as follows:

1. A separate simulation and superposition analysis method of the excavation stress field and rainfall seepage field is proposed. Meanwhile, the stress uncertainty problem caused by the excavation of shallow saturated slopes formed by continuous rainfall is solved, and simulation of alternating slope excavation and rainfall is realised. Moreover, taking an actual slope project as a field study, the safety factor range of slope stability influenced by rainfall is obtained through back analysis. Then, the limit equilibrium method is used to invert the rock and soil shear strength parameters. After that, the proposed method is applied to numerically study the slope failure mechanism under alternating excavation and rainfall conditions. The results show that the proposed method can appropriately reproduce the slope deformation and failure process, and its effectiveness and accuracy are fully verified.
2. Excavation and rainfall were two main factors that induced the two sliding failures of the AK2 + 210 ~ AK2 + 610 section slope. On the one hand, the excavation unloading triggered stress adjustment. On the other hand, the exposed surface provided rainwater infiltration channels. Meanwhile, the rainfall-generated pore water pressure further changed the slope stress state and produced transient saturated zones that reduced the shear strength and increased the bulk density of the slope. This process was the direct cause of the two sliding failures. Hence, when constructing soft rock slopes in rainy areas, the excavation slope ratio should be controlled to prevent the excavated toe from being damaged. Additionally, attention should be paid to the weather to avoid excavating during the rainy

season. Before rainfall, waterproofing and drainage measures should be taken to prevent the formation of an “excavation disturbance + rainfall infiltration” disaster chain.

3. Considering that slope sliding mainly occurred in the upper third to fifth-level slopes and the two failures were both caused by the traction of the excavated slope toe under rainfall, a comprehensive measure of “sprayed concrete protection + plain concrete protection wall + anchor lattice beam” is therefore suggested in this study. First, because the deformation induced by rainfall will greatly increase the difficulty of applying slope treatments and delay the construction progress, sprayed concrete can be applied to seal the modified excavation surface to block rainfall infiltration quickly and provide a construction environment for subsequent stabilization measures. Second, the wide second platform can be utilised to set a plain concrete protection wall in front of the third-level slope to completely prevent rainwater infiltration and load the slope toe to avoid traction-sliding failures. Finally, the use of anchor lattice beam support at the fourth- and fifth-level slopes can effectively control the shallow sliding deformation. These findings and suggestions can provide a treatment reference for other slope projects experiencing alternating excavation and rainfall disturbance.

**Funding** This work was financially supported by the China Postdoctoral Science Foundation (Grant No. 2020M680950) and the National Natural Science Foundation of China (Grant No. 51627804), for which the authors are grateful.

**Data availability** Available on reasonable request.

## Declarations

**Conflict of interest** The authors declare no competing interests.

## References

- Bishop AW (1959) The principle of effective stress. *Tecknisk Ukeblad* 106(39):859–863
- Bishop AW, Blight GE (1963) Some aspects of effective stress in saturated and unsaturated soil. *Geotech* 13(3):177–197
- Fredlund D G (1998) Bringing unsaturated soil mechanics into engineering practice. *Proceedings of the 2nd international conference on unsaturated soil* 2(36):2–51
- Fu CD, Sheng Q, Li G, Zhang ZP, Zhou YQ, Du YX (2020) Analysis of landslide stability under seismic action and subsequent rainfall: a case study on the Ganjiazhai giant landslide along the Zhaotong-Qiaojia road during the 2014 Ludian earthquake, Yunnan. *China Bull Eng Geol Environ* 79(10):5229–5248
- Han H, Shi B, Zhang L (2021) Prediction of landslide sharp increase displacement by SVM with considering hysteresis of groundwater change. *Eng Geol* 280(2021):105876
- Ishii Y, Ota K, Kuraoka S, Tsunaki R (2012) Evaluation of slope stability by finite element method using observed displacement of landslide. *Landslides* 9(3):335–348
- Jiang ZM, Wu ZC, Feng SC, Zhong HY, Wang JY, Wang GY (2015) Limit equilibrium method for stability analysis of slope with transient saturated area. *J Hydraul Eng* 46(7):773–782
- Jotisankasa A, Coop M, Ridley A (2009) The mechanical behaviour of an unsaturated compacted silty clay. *Geotechnique* 59(5):415–428
- Kim Y, Jeong S, Kim J (2016) Coupled infiltration model of unsaturated porous media for steady rainfall. *Soils Found* 56(6):1071–1081
- Li CD, Fu ZY, Wang Y, Tang HM, Yan JF, Gong WP, Yao WM, Criss RE (2019) Susceptibility of reservoir-induced landslides and strategies for increasing the slope stability in the Three gorges reservoir area: Zigui basin as an example. *Eng Geol* 261:105279
- Lin F, Wu LZ, Huang RQ, Zhang H (2018) Formation and characteristics of the Xiaoba landslide in Fuquan, Guizhou. *China Landslides* 15(4):669–681
- Li Q, Wang YM, Zhang KB, Yu H, Tao ZY (2020) Field investigation and numerical study of a siltstone slope instability induced by excavation and rainfall. *Landslides* 17(6):1485–1499
- Liu JM, Qiu Y, Guo TT, Song WZ, Gu C (2020) Comparative experimental study on static shear strength and postcyclic strength of saturated silty clay. *Rock Soil Mech* 41(3):773–780
- Liu JX, Yang C, Gan J, Liu Y, Wei L, Xie Q (2017) Stability analysis of road embankment slope subjected to rainfall considering runoff-unsaturated seepage and unsaturated fluid–solid coupling. *Int J Civ Eng* 15(6):865–876
- Li ZQ, Xue YG, Li SC, Zhang LW, Wang D, Li B, Zhang W, Ning K, Zhu JY (2017) Deformation features and failure mechanism of steep rock slope under the mining activities and rainfall. *J Mt Sci-Engl* 14(1):31–45
- Lu N, Sener-Kaya B, Wayllace A, Godt JW (2012) Analysis of rainfall-induced slope instability using a field of local factor of safety. *Water Resour Res* 48(9):9524
- Nguyen VU (1984) Back calculations of slope failures by the secant method. *Geotechnique* 34(3):423–427
- Oh S, Lu N (2015) Slope stability analysis under unsaturated conditions: case studies of rainfall-induced failure of cut slopes. *Eng Geol* 184:96–103
- Potts DM, Zdravkovic L (1999) *Finite element analysis in geotechnical engineering: theory*. Thomas Telford, London, UK:72–73.
- Qiu X, Jiang HB, Ou J (2020) Numerical analysis of formation conditions and evolution characteristics of transient saturation zone of a slope under rainfall conditions. *J Hydraul Eng* 51(12):1525–1535
- Robinson JD, Vahedifard F, AghaKouchak A (2017) Rainfall-triggered slope instabilities under a changing climate: comparative study using historical and projected precipitation extremes. *Can Geotech J* 54(1):117–127
- Shinoda M, Miyata Y, Kurokawa U, Kondo K (2019) Regional landslide susceptibility following the 2016 Kumamoto earthquake using back-calculated geomaterial strength parameters. *Landslides* 16(8):1497–1516
- Sun HY, Pan P, Lu Q, Wei ZL, Xie W, Zhan W (2019) A case study of a rainfall-induced landslide involving weak interlayer and its treatment using the siphon drainage method. *Bull Eng Geol Environ* 78(6):4063–4074
- Taga H, Turkmen S, Kacka N (2015) Assessment of stability problems at southern engineered slopes along mersin-tarsus motorway in turkey. *Bull Eng Geol Environ* 74(2):379–391
- Tang X, Chen JP, Liu DG, Xu N (2015) The relationship between microstructure characteristics and shear strength of tuff soil landslide zone. *Electron J Geotech Eng* 20(10):4151–4163
- Tan HD, Jian WX, Lu Y, Song Y (2018) Hedro-mechanical Interaction Characteristics of the Tuff Residual Soil in South Jiangxi Province of China. *Safety and Environ Eng* 25(1):18–22

- Wang H, Wang XD, Pan J (2017) A case study of super-high cut slope I: simulation and analysis of instability mechanism of slopes. *Chin J Rock Mech Eng-En* 4:125–135
- Wang JJ, Liang Y, Zhang HP, Wu Y, Lin X (2014) A loess landslide induced by excavation and rainfall. *Landslides* 11(1):141–152
- Yang DH, Yan RT, Wei CF, Zhang M, Zhang Q (2016) A study of water chemical sensitivity of strength indices of silty clay. *Rock Soil Mech* 37(12):3529–3536
- Zhang CY, Zhang M, Zhang TL, Dai ZW, Wang LQ (2020) Influence of intrusive granite dyke on rainfall-induced soil slope failure. *Bull Eng Geol Environ* 79(10):5259–5276
- Zhao L, Li D, Tan H, Cheng X, Zuo S (2019) Characteristics of failure area and failure mechanism of a bedding rockslide in Libo county, Guizhou. *China Landslides* 16(7):1367–1374
- Zhao RX, Yin YP, Li B, Wang WP (2017) Research on the colluvial landslide stability during reservoir water level fluctuation. *J Hydraulic Eng* 48(4):435–445
- Zhuang JQ, Peng JB (2014) A coupled slope cutting-a prolonged rainfall-induced loess landslide: a 17 October 2011 case study. *Bull Eng Geol Environ* 73(4):997–1011
- Zuo C, Liu D, Ding S, Chen J (2016) Micro-characteristics of strength reduction of tuff residual soil with different moisture. *KSCE J Civ Eng* 20(2):639–646